

Real-time Measurement of Nanotube Resonator Fluctuations in an Electron Microscope

I. Tsoutsios^{1,*}, A. Tavernarakis^{1,*}, J. Osmond¹, P. Verlot^{1,2,†} and A. Bachtold¹

¹ICFO-Institut de Ciències Fotoniques,

The Barcelona Institute of Science and Technology, 08860 Castelldefels (Barcelona), Spain

²Université Claude Bernard Lyon 1, UCBL,

Domaine Scientifique de La Doua, 69622 Villeurbanne, France

November 26, 2016

1 Effect of the electron beam intensity in scanning mode

In this section, we consider the possible influence of the electron beam intensity on the motion statistic as measured in scanning mode. For simplicity, the following discussion will be performed in the one-dimensional case, without restricting generality.

The average intensity $\bar{I}(x)$ received by the carbon nanotube resonator of diameter d expresses as:

$$\bar{I}(x) = d \int_{-\infty}^{+\infty} dy I^{\text{in}}(y) \mathcal{P}(x - y), \quad (1)$$

with $I^{\text{in}}(y) = \frac{I_0}{\sqrt{2\pi w_0}} e^{-\frac{y^2}{2w_0}}$ denoting the (Gaussian) intensity profile of the electron beam (e-beam) (I_0 the e-beam intensity, w_0 the e-beam waist), \mathcal{P} the position probability density function (PDF) of the carbon nanotube resonator and x the position of the electron beam, relative to the equilibrium position of the nanotube (see Fig. S1). For e-beam waists small compared to the motion variance $\sigma \gg w_0$, Eq. 1 simplifies as:

$$\bar{I}(x) \simeq dI_0 \mathcal{P}(x). \quad (2)$$

In particular, it follows from Eq. 2 that the averaged secondary electron emission $\bar{I}_{\text{SE}} = \beta \bar{I}(x)$ (with β the secondary electron yield) is proportional to the motion PDF of the nanotube resonator, which we use in our work in order to calibrate our devices [1, 2]. Importantly, such calibration prominently relies on the assumption that the carbon nanotube resonator remains at thermal equilibrium. However, due to their extremely reduced dimensions, the dynamics of carbon nanotube resonators may be affected by the electron beam itself. In the following, we show that such effects result in strong modifications of the effectively measured motion PDF, which are not observed with our carbon nanotube resonators, ensuring that the dominant source of excitation is of a thermal origin.

Assuming that the nanomechanical motion is driven by the electron beam implies a dependence of the PDF with respect to the average absorption rate, $\bar{I}(x) \simeq dI_0 \mathcal{P}(x, \bar{I}(x))$, describing a multistable system in general. This behaviour can be understood as follows: The driving strength of the electron beam is proportional to the electron absorption rate, which increases with the probability to find the nanotube resonator within the electron beam, as shown by Eq. 2. If we assume that the nanotube resonator is initially staying at thermal equilibrium with motion variance σ_{th} (Fig. S1(b-0)), the electron beam exposure is maximized at the center of the thermal trajectory, where the thermal motion PDF is peaking (Fig. S1(b-1)). The effect of the electron beam is to increase the motion variance to σ_{el} , that is to spread the motion PDF, which subsequently results in a drastic decrease of the electron absorption rate (Fig. S1(b-2)). The effect of the electron beam being reduced at this point, the nanotube resonator returns to its thermal equilibrium: Therefore, the dynamics of nanotube resonator switches back and forth between the two states (1) and (2), where it is alternately driven by the electron beam.

*These authors contributed equally

†Corresponding author; Email: pierre.verlot@univ-lyon1.fr

To give a more quantitative description of the expected dynamics in presence of electron beam driving, we further assume the e-beam driven nanomechanical state to remain Gaussian, with corresponding PDF \mathcal{P} written as:

$$\mathcal{P}(x, \bar{I}(x)) = \frac{1}{\sqrt{2\pi}\sigma[\bar{I}(x)]} \exp \left\{ -\frac{x^2}{2\sigma^2[\bar{I}(x)]} \right\}, \quad (3)$$

with $\sigma[I(x)] = \sigma_{\text{th}}\sqrt{1 + \frac{\mathcal{P}(x)}{\mathcal{P}_{\text{th}}(0)}\xi_e}$ the motion variance. Here $\mathcal{P}_{\text{th}}(x)$ denotes the thermal PDF and ξ_e the e-beam to thermal forces spectral densities ratio¹. Eq. 3 can be solved by means of a perturbative approach. Writing $\mathcal{P}(x)$ as the sum of the thermal PDF plus a correction, $\mathcal{P}(x) = \mathcal{P}_{\text{th}}(x) + \tilde{\mathcal{P}}(x)$, one obtains to first order in ξ_e :

$$\tilde{\mathcal{P}}(x) \simeq -\sqrt{\frac{\pi}{2}}\xi_e \left(1 - \frac{x^2}{2\sigma_{\text{th}}^2} \right) \sigma_{\text{th}} \mathcal{P}_{\text{th}}^2(x). \quad (4)$$

Fig. S1(c) shows the theoretically expected motion PDF $\mathcal{P}(x) = \mathcal{P}_{\text{th}}(x) + \tilde{\mathcal{P}}(x)$ for increasing values of ξ_e . Fig. S1(c-i) shows the unchanged (thermal) PDF in absence of e-beam drive ($\xi_e = 0$). Fig. S1(c-ii) shows the modified PDF for $\xi_e = 0.5$, that is when e-beam drive contributes to 1/3 of the total motion fluctuations. The corresponding distribution is strongly deformed, showing important flattening and broadening. Fig. S1(c-iii) and S1(c-iv) show the theoretical expectation for the measured motion PDF for $\xi_e = 1$ and $\xi_e = 1.5$. An increasing splitting is observed, which is a manifestation of the above described scenario: The nanotube resonator tends to escape the central region, where e-beam driving is larger. Note that further predicting the evolution of $\tilde{\mathcal{P}}(x)$ at higher ebeam strength requires expanding Eq. 3 to higher orders, resulting in the appearance of multiple solutions around the central region, which accounts for the above mentioned multistable behaviour.

To verify the influence of the electron beam on the motion PDF, we have realized a series of images acquired at various input current. The resulting PDF where found to remain of a Gaussian nature, with no significant distortion being observed, which is a first indication that e-beam driving effects are negligible. Moreover, fitting the width of the PDF enables a quantitative determination of the motion variance, as already discussed in the main manuscript. The results are shown on Fig. S1(d), demonstrating that the motion variance remains constant (within the measurement uncertainties) while increasing the interaction time between the mechanical vibrations and the electron beam over more than two decades. We therefore conclude that the effect of the electron beam remains negligible, the observed fluctuations being of a thermal origin.

2 Estimation of the diameters of carbon nanotube resonators

To estimate the diameter of our carbon nanotube resonators, we follow the protocol introduced in the work from Krishnan et al. in Ref [3]. Indeed, the motion variance σ_{th} (as obtained via the Secondary Electrons (SEs) images, see the main text) can be further related to the physical parameters of the nanotubes via the expression [3]:

$$\sigma_{\text{th}}^2 = 0.1061 \frac{L^3 k_B T}{Y r^3 G}, \quad (5)$$

with L the length of the nanotube, k_B Boltzmann's constant, T the temperature, Y Young's modulus, r the radius of the nanotube and G its wall thickness. Therefore, in the case of device D1, we have measured $\sigma_{\text{th}} = 14 \text{ nm}$ and $L = 1.2 \mu\text{m}$; assuming a Young's modulus $Y = 1.25 \text{ TPa}$ [3] and a single wall nanotube thickness $G = 0.34 \text{ nm}$, we finally obtain a radius $r = 2 \text{ nm}$.

3 One dimensional Brownian motion of a carbon nanotube resonator

In this section we describe the statistical behaviour of a thermally driven carbon nanotube resonator in one of its vibrational direction. Figure S2 (a) shows the displacement power spectrum associated with the in-plane fundamental mechanical resonance of device D1. Figure S2 (b) shows the corresponding motion quadratures in the phase-space. Figure S2 (c) shows histograms associated with each quadrature. Straight lines correspond to Gaussian fits. In total, the quadratures of the in-plane fundamental mode undergo a Gaussian distributed random walk in the phase space, which defines the Brownian motion of a harmonic resonator.

¹Note that defined as such, $S_F^{\text{el}} = \xi_e S_F^{\text{th}}$ (S_F^{th} the thermal force noise spectral density) corresponds to the equivalent e-beam force noise spectral density required for driving the carbon nanotube resonator into a Gaussian state with variance $\sigma_{\text{rl}} = \sqrt{\xi_e} \sigma_{\text{th}}$

4 Energy autocorrelation function of a noise driven harmonic oscillator

In this section, we derive the expression of the energy autocorrelation function $C_{\mathcal{E}}(t, t + \tau) = \langle \mathcal{E}(t)\mathcal{E}(t + \tau) \rangle$, with $\mathcal{E}(t) = X_1^2(t) + X_2^2(t)$ the mechanical energy, $X_{1,2}(t)$ the motion quadratures, and where $\langle \dots \rangle$ denotes statistical averaging over the driving external bath. In the following, we will assume the mechanical oscillator to be driven by a stationary, Gaussian bath.

We start with calculating the second moment autocorrelation function $C_{X^2}(t, t + \tau) = \langle X^2(t)X^2(t + \tau) \rangle$ associated with one given quadrature X (the mechanical motion being assumed to be driven by a Gaussian noise, this expression will be identical for any given motion quadrature). For a high-Q harmonic oscillator, the time evolution of such quadrature corresponds to the convolution between the quadrature impulse response $\chi(t)$ and an effective Gaussian driving noise $F_X^{\text{th}}(t)$ such that $\langle F_X^{\text{th}}(t)F_X^{\text{th}}(t') \rangle = 2S_F^{\text{th}}\delta(t' - t)$ (S_F^{th} the single sideband force spectral density associated with the external driving bath, and δ the Dirac delta function):

$$X(t) = \int_{-\infty}^{+\infty} dt_1 \chi(t - t_1) F_X^{\text{th}}(t_1) \quad (6)$$

$$\chi(t) = \frac{1}{2M\Omega_M} \Theta(t) e^{-\frac{\Gamma_M}{2}t}, \quad (7)$$

with M , Ω_M , and Γ_M the mass, mechanical resonance frequency and mechanical damping rate of the oscillator, and with Θ denoting the Heaviside step function. Assuming the stationary nature of the problem, all correlation functions are time independent, $C_{X^2}(t, t + \tau) = C_{X^2}(0, \tau) = C_{X^2}(\tau)$. Using Eqs. 6 and 7, this autocorrelation function can be subsequently expanded as:

$$\begin{aligned} C_{X^2}(\tau) &= \langle X^2(0)X^2(\tau) \rangle \\ &= \langle \left(\int_{-\infty}^{+\infty} dt_1 \chi(-t_1) F_X^{\text{th}}(t_1) \right)^2 \left(\int_{-\infty}^{+\infty} dt_2 \chi(\tau - t_2) F_X^{\text{th}}(t_2) \right)^2 \rangle \\ &= \langle \iint \int_{[-\infty, +\infty]^4} dt_1 dt_2 dt_3 dt_4 \chi(-t_1) \chi(-t_2) \chi(\tau - t_3) \chi(\tau - t_4) F_X^{\text{th}}(t_1) F_X^{\text{th}}(t_2) F_X^{\text{th}}(t_3) F_X^{\text{th}}(t_4) \rangle \\ &= \iint \int_{[-\infty, +\infty]^4} dt_1 dt_2 dt_3 dt_4 \chi(-t_1) \chi(-t_2) \chi(\tau - t_3) \chi(\tau - t_4) \langle F_X^{\text{th}}(t_1) F_X^{\text{th}}(t_2) F_X^{\text{th}}(t_3) F_X^{\text{th}}(t_4) \rangle, \end{aligned} \quad (8)$$

where the integrals and statistical average have been swapped between the third and last steps because of the stationarity of the problem. To determine the value of the quadruplet $\langle F_X^{\text{th}}(t_1)F_X^{\text{th}}(t_2)F_X^{\text{th}}(t_3)F_X^{\text{th}}(t_4) \rangle$, we use Wick's theorem², which states that it can be rewritten as the sum of all possible binomial contractions of its components:

$$\begin{aligned} \langle F_X^{\text{th}}(t_1)F_X^{\text{th}}(t_2)F_X^{\text{th}}(t_3)F_X^{\text{th}}(t_4) \rangle &= \langle F_X^{\text{th}}(t_1)F_X^{\text{th}}(t_2) \rangle \langle F_X^{\text{th}}(t_3)F_X^{\text{th}}(t_4) \rangle + \langle F_X^{\text{th}}(t_1)F_X^{\text{th}}(t_3) \rangle \langle F_X^{\text{th}}(t_2)F_X^{\text{th}}(t_4) \rangle \\ &\quad + \langle F_X^{\text{th}}(t_1)F_X^{\text{th}}(t_4) \rangle \langle F_X^{\text{th}}(t_2)F_X^{\text{th}}(t_3) \rangle \end{aligned} \quad (9)$$

Using that $\langle F_X^{\text{th}}(t)F_X^{\text{th}}(t') \rangle = 2S_F^{\text{th}}\delta(t' - t)$, we finally obtain:

$$\begin{aligned} C_{X^2}(\tau) &= 4(S_F^{\text{th}})^2 \iint \int_{[-\infty, +\infty]^4} dt_1 dt_2 dt_3 dt_4 \chi(-t_1) \chi(-t_2) \chi(\tau - t_3) \chi(\tau - t_4) \times \\ &\quad \times (\delta(t_2 - t_1)\delta(t_4 - t_3) + \delta(t_3 - t_1)\delta(t_4 - t_2) + \delta(t_4 - t_1)\delta(t_3 - t_2)). \end{aligned} \quad (10)$$

It is therefore straight to simplify Eq. 10 to obtain:

$$\frac{1}{4(S_F^{\text{th}})^2} C_{X^2}(\tau) = \iint_{[-\infty, +\infty]^2} dt_1 dt_3 \chi^2(-t_1) \chi^2(\tau - t_3) + 2 \left(\int_{-\infty}^{+\infty} dt_1 \chi(-t_1) \chi(\tau - t_1) \right)^2. \quad (11)$$

²Indeed, Wick's theorem applies, F_X^{th} being a Gaussian, centered statistical variable

The two terms on the right side of Eq. 11 can be straight forwardly computed:

$$\iint_{[-\infty, +\infty]^2} dt_1 dt_3 d\chi^2(-t_1) \chi^2(\tau - t_3) = \left(\frac{1}{2M\Omega_M} \right)^4 \times \frac{1}{\Gamma_M^2}, \quad (12)$$

$$\left(\int_{-\infty}^{+\infty} dt_1 \chi(-t_1) \chi(\tau - t_1) \right)^2 = \left(\frac{1}{2M\Omega_M} \right)^4 \times \frac{1}{\Gamma_M^2} e^{-\Gamma_M |\tau|}, \quad (13)$$

and finally:

$$C_{X^2}(\tau) = 4 \left(\frac{1}{2M\Omega_M} \right)^4 \left(\frac{S_F^{\text{th}}}{\Gamma_M} \right)^2 \left(1 + 2e^{-\Gamma_M |\tau|} \right). \quad (14)$$

We now resume and terminate the calculation of the energy autocorrelation function $C_E(\tau) = C_E(0, \tau) = \langle (X_1^2(0) + X_2^2(0)) (X_1^2(\tau) + X_2^2(\tau)) \rangle$, which can be expanded as:

$$C_E(\tau) = \langle X_1^2(0) X_1^2(\tau) \rangle + \langle X_2^2(0) X_2^2(\tau) \rangle + \langle X_1^2(0) X_2^2(\tau) \rangle + \langle X_2^2(0) X_1^2(\tau) \rangle. \quad (15)$$

The first two terms in Eq. 15 are identical and are given by Eq. 14, whereas $\langle X_i^2(0) X_j^2(\tau) \rangle_{i \neq j} = \langle X_i^2(0) \rangle \times \langle X_j^2(\tau) \rangle = \langle X^2 \rangle^2$, due to the uncorrelated nature of X_1 and X_2 and to the isotropic distribution of the driving fluctuations. Finally, we obtain:

$$\begin{aligned} C_E(\tau) &= 2(C_{X^2}(\tau) + \langle X^2 \rangle^2) \\ &= 4 \left(\frac{k_B T}{M\Omega_M^2} \right)^2 \left(1 + e^{-\Gamma_M |\tau|} \right), \end{aligned} \quad (16)$$

where we have assumed the driving bath to be of a thermal nature with temperature T , $S_F^{\text{th}} = 2M\Gamma_M k_B T$, yielding to $\langle X^2 \rangle = k_B T / M\Omega_M^2$. Eq. 16 shows that the energy autocorrelation function is an exponentially decaying function of time, with a time constant $1/\Gamma_M$.

5 Two-modes energy autocorrelation

For suspended nanomechanical cantilevers, the mechanical mode of interest comes along with a second mechanical mode associated with the perpendicular direction of vibration. In the frame rotating at the mechanical resonance frequency Ω_1 associated with mode 1, the quadratures of the mechanical signal I and Q can be therefore expressed as:

$$I(t) = \frac{1}{2} (X_{11}(t) + X_{21}(t) \cos \Delta\Omega t) + \frac{1}{2} X_{22}(t) \sin \Delta\Omega t, \quad (17)$$

$$Q(t) = -\frac{1}{2} X_{21}(t) \sin \Delta\Omega t + \frac{1}{2} (X_{12}(t) + X_{22}(t) \cos \Delta\Omega t) \quad (18)$$

where $X_{ij}(t)$ denote the j^{th} quadrature associated with mode i and with $\Delta\Omega = \Omega_1 - \Omega_2$ the frequency splitting between the two mechanical modes. The "energy" as obtained from I and Q , $\tilde{\mathcal{E}}(t) = I^2(t) + Q^2(t)$ is given by:

$$\begin{aligned} \tilde{\mathcal{E}}(t) &= \mathcal{E}_1(t) + \mathcal{E}_2(t) + 2(X_{11}(t)X_{21}(t) + X_{12}(t)X_{22}(t)) \cos \Delta\Omega t \\ &\quad + 2(X_{11}(t)X_{22}(t) - X_{21}(t)X_{12}(t)) \sin \Delta\Omega t, \end{aligned} \quad (19)$$

where we have noted $\mathcal{E}_i(t) = X_{i1}^2(t) + X_{i2}^2(t)$ the energy of mode i . The autocorrelation $C_{\tilde{\mathcal{E}}}(\tau) = \langle \tilde{\mathcal{E}}(t) \tilde{\mathcal{E}}(t + \tau) \rangle$ therefore reads:

$$\begin{aligned} \langle \tilde{\mathcal{E}}(0) \tilde{\mathcal{E}}(\tau) \rangle &= C_{\mathcal{E}_1}(\tau) + C_{\mathcal{E}_2}(\tau) \\ &\quad + 2\langle (X_{11}(0)X_{21}(0) + X_{12}(0)X_{22}(0))(X_{11}(\tau)X_{21}(\tau) + X_{12}(\tau)X_{22}(\tau)) \rangle \cos \Delta\Omega \tau \\ &= C_{\mathcal{E}_1}(\tau) + C_{\mathcal{E}_2}(\tau) + 4(C_{11}(\tau)C_{21}(\tau) + C_{12}(\tau)C_{22}(\tau)) \cos \Delta\Omega \tau, \end{aligned} \quad (20)$$

with $C_{ij}(\tau) = \langle X_{ij}(0)X_{ij}(\tau) \rangle$. To obtain Eq. 20, we have utilized the stationarity of the problem ($\langle \tilde{\mathcal{E}}(t) \tilde{\mathcal{E}}(t + \tau) \rangle = \langle \tilde{\mathcal{E}}(0) \tilde{\mathcal{E}}(\tau) \rangle$), and we have assumed modes 1 and 2 to be perfectly uncorrelated, $\langle X_{ij}(0)X_{kl}(\tau) \rangle = \delta_{ik}\delta_{jl}C_{ij}(\tau)$ (δ the Kronecker delta symbol). Thereby, Eq. 20 shows that the two-modes energy autocorrelation function writes as

the sum of the individual energy autocorrelation functions, plus a beat signal at the splitting frequency $\Delta\Omega$. Note that even for negligible splitting ($\delta\Omega \ll \Gamma_1, \Gamma_2$), separating the contributions of each mode remains possible as long as they have distinct mechanical decay rates, which is often the case. Indeed, the sum of the two first terms in Eq. 20 is no longer a purely exponentially decaying function of time, and the deviations from this model therefore enable to accurately address the presence of 2 modes and their corresponding quality factors through the slope irregularities. Note that this would not be equivalent to possible Lorentzian irregularities in the motion spectrum, which is subjected to frequency noise (see below) and does not enable damping extraction to the same level of accuracy.

6 Energy autocorrelation in presence of frequency noise

A widely known advantage of extracting the dissipation properties from the autocorrelation function of the energy is that it is immune to unavoidable sources of frequency noise [4], which becomes critical in the ultra-high Q-factor regime [5, 6]. To establish this fact, we assume the motion quadratures to be demodulated at a frequency $\Omega_d \neq \Omega_M$:

$$\begin{aligned} I(\Omega_d, t) &= (F * \tilde{I})(t) \\ Q(\Omega_d, t) &= (F * \tilde{Q})(t) \end{aligned} \quad (21)$$

$$\begin{aligned} \tilde{I}(\Omega_d, t) &= x(t) \times \cos \Omega_d t \\ \tilde{Q}(\Omega_d, t) &= x(t) \times \sin \Omega_d t, \end{aligned} \quad (22)$$

where $F*$ denotes low pass filtering convolution, and $x(t)$ the time evolution of mechanical motion. We subsequently write the mechanical motion in terms of its intrinsic quadratures, $x(t) = X_1(t) \cos \Omega_M t + X_2(t) \sin \Omega_M t$. It is therefore straight forward to expand Eqs. 22:

$$\begin{aligned} \tilde{I}(\Omega_d, t) &= \frac{1}{2} [\cos(\Omega_M - \Omega_d)t + \cos(\Omega_M + \Omega_d)t] X_1(t) + \frac{1}{2} [\sin(\Omega_M + \Omega_d)t + \sin(\Omega_M - \Omega_d)t] X_2(t) \\ \tilde{Q}(\Omega_d, t) &= \frac{1}{2} [\sin(\Omega_M + \Omega_d)t - \sin(\Omega_M - \Omega_d)t] X_1(t) + \frac{1}{2} [\cos(\Omega_M - \Omega_d)t - \cos(\Omega_M + \Omega_d)t] X_2(t). \end{aligned} \quad (23)$$

The filtering essentially result in suppression of rapid signal components in \tilde{I} and \tilde{Q} . Assuming that $|\Omega_M - \Omega_d| \ll \Omega_M$, Eqs. 21 can therefore be simplified to:

$$\begin{aligned} I(\Omega_d, t) &= \frac{1}{2} X_1(t) \cos(\Omega_M - \Omega_d)t + \frac{1}{2} X_2(t) \sin(\Omega_M - \Omega_d)t \\ Q(\Omega_d, t) &= -\frac{1}{2} X_1(t) \sin(\Omega_M - \Omega_d)t + \frac{1}{2} X_2(t) \cos(\Omega_M - \Omega_d)t. \end{aligned} \quad (24)$$

The energy can therefore be estimated in the referential rotating at frequency Ω_d :

$$\begin{aligned} \mathcal{E}(\Omega_d, t) &= I^2(t) + Q^2(t) \\ &= \frac{1}{4} X_1^2(t) \cos^2(\Omega_M - \Omega_d)t + \frac{1}{4} X_2^2(t) \sin^2(\Omega_M - \Omega_d)t \\ &\quad + \frac{1}{2} X_1(t) X_2(t) \cos(\Omega_M - \Omega_d)t \sin(\Omega_M - \Omega_d)t \\ &\quad + \frac{1}{4} X_1^2(t) \sin^2(\Omega_M - \Omega_d)t + \frac{1}{4} X_2^2(t) \cos^2(\Omega_M - \Omega_d)t \\ &\quad - \frac{1}{2} X_1(t) X_2(t) \cos(\Omega_M - \Omega_d)t \sin(\Omega_M - \Omega_d)t \\ &= \frac{1}{4} [X_1^2(t) + X_2^2(t)]. \end{aligned} \quad (25)$$

Eq. 25 therefore shows that the energy does not depend of the demodulation procedure. In particular, this result holds even in presence of frequency noise, that is for $\Omega_M = \Omega_d + \delta\Omega(t)$, with $\delta\Omega(t)$ a slowly varying frequency noise term.

7 2-dimensional nanomechanical response

In this part we take into account the 2-dimensional motional nature of the carbon nanotube resonator, that is its ability to vibrate along two perpendicular directions ($\mathbf{e}_1, \mathbf{e}_2$). In this basis, Newton's law can be written as:

$$\begin{aligned} M_{\text{eff}} \frac{d^2x_1}{dt^2} &= -k_1 x_1(t) - M_{\text{eff}} \Gamma_1 \frac{dx_1}{dt} + \mathbf{F}_{\text{el}}(t) \cdot \mathbf{e}_1 + F_{\text{th},1}(t) \\ M_{\text{eff}} \frac{d^2x_2}{dt^2} &= -k_2 x_2(t) - M_{\text{eff}} \Gamma_2 \frac{dx_2}{dt} + \mathbf{F}_{\text{el}}(t) \cdot \mathbf{e}_2 + F_{\text{th},2}(t), \end{aligned} \quad (26)$$

with $x_{1,2}(t)$ the motion trajectories along directions $\mathbf{e}_{1,2}$, $k_{1,2}$ and $\Gamma_{1,2}$ the effective spring constants and linear damping rates associated with displacements $x_{1,2}$, $F_{\text{th}\{1,2\}}$ the (uncorrelated) thermal forces in the eigendirections of motion, and \mathbf{F}_{el} the (random) force exerted by the electron beam onto the nanotube resonator. Noting $\beta = (\mathbf{e}_1, \mathbf{F}_{\text{el}})$ the angle between the first motional eigendirection and the electron beam induced force, the stationary solutions of Eqs. 26 write in Fourier space:

$$\begin{aligned} x_1[\Omega] &= \chi_1[\Omega] (\cos \beta F_{\text{el}}[\Omega] + F_{\text{th},1}[\Omega]) \\ x_2[\Omega] &= \chi_2[\Omega] (-\sin \beta F_{\text{el}}[\Omega] + F_{\text{th},2}[\Omega]), \end{aligned} \quad (27)$$

with Ω the Fourier frequency, $\chi_{1,2}[\Omega] = 1/M_{\text{eff}}(\Omega_{1,2}^2 - \Omega^2 - i\Gamma_{1,2}\Omega)$ the mechanical susceptibilities associated with modes 1 and 2 ($\Omega_{1,2}^2 = k_{1,2}/M_{\text{eff}}$ the mechanical resonance frequencies), and $F_{\text{el}} = \|\mathbf{F}_{\text{el}}\|$.

Our detection scheme projects the 2-dimensional nanomechanical motion onto a given direction \mathbf{u}_m along which the linear displacement sensitivity becomes maximum [7]. The measured signal is subsequently proportional to the projected displacements x_θ given by:

$$x_\theta(t) = \cos \theta x_1(t) - \sin \theta x_2(t), \quad (28)$$

with $\theta = \mathbf{e}_1 \cdot \mathbf{u}_m$. Combining Eqs. 27 and 28 enables to derive the output fluctuation spectrum $2\pi\delta[\Omega' + \Omega]S_\theta[\Omega] = \langle x_\theta[\Omega]x_\theta[\Omega'] \rangle$ (δ denoting the Dirac delta function and $\langle \dots \rangle$ statistical averaging):

$$\begin{aligned} S_\theta[\Omega] &= \cos^2 \theta |\chi_1[\Omega]|^2 S_{F,1}^{\text{th}}[\Omega] + \sin^2 \theta |\chi_2[\Omega]|^2 S_{F,2}^{\text{th}}[\Omega] \\ &\quad + \frac{1}{2} |\chi_1[\Omega](2 \cos^2 \theta \cos \beta + \sin 2\theta \sin \beta) + \chi_2[\Omega](2 \sin^2 \theta \cos \beta - \sin 2\theta \sin \beta)|^2 S_F^{\text{el}}[\Omega]. \end{aligned} \quad (29)$$

The two first terms in Eq. 29 correspond to the (uncorrelated) thermal contributions of mode 1 and 2 as projected in the direction defined by \mathbf{u}_m : In absence of any further driving term, one retrieves the usual result that linear motion detection yields to a composite spectrum whose peak amplitudes enables to determine the relative orientations of the eigenaxis of vibration [7, 8, 9]. Instead, the second line in Eq. 29 shows that the driving contribution arising from the e-beam fluctuations features the *coherent* sum of the mechanical response, where the relative phase of their response towards the e-beam noise is partially preserved: Contrary to thermal excitations, which are by nature uncorrelated along the eigen axis of vibration, the electron beam as a driving bath creates motion correlations that are characteristic of the common origin of the fluctuations when observed in two perpendicular transduction directions.

It is difficult to favour one particular mechanism that could be the dominant contribution to the electron beam backaction. In the perfect, Heisenberg limited probe case, the backaction is expected to exert along the optimal detection direction \mathbf{u}_m . However quantum backaction mechanisms remain to be further investigated in the present case of electron beam assisted detection of nanotube resonators, and we prefer not to make any definitive assumption at this stage and to leave the quantum backaction force orientation (as defined by the angle β) as a free parameter. Fig. S3 shows the evolution of the composite spectrum $S_\theta[\Omega]$ for 4 different values of β covering the forward half plane ($\beta = 0^\circ, 45^\circ, 90^\circ$, and 135° from Fig. S3(a) to SS3(d)). Each subset shows the backaction free case ($S_F^{\text{el}} = 0$, in blue) together with the full spectrum as computed from Eq. 29 (in yellow, with $S_F^{\text{el}} = 100S_{F,\{1,2\}}^{\text{th}}$), for various orientations of the eigenaxis of vibration with respect to the optimal detection direction \mathbf{u}_m ($\theta = 0^\circ$ to $\theta = 160^\circ$ from (i) to (ix)). The spectra have been normalized in order to better appreciate the differences induced by the presence of e-beam driving. One sees that measuring one of the eigenvibration along the optimal detection direction ($\theta = 0^\circ$) does not enable to spectrally distinguish the thermally driven case from the e-beam driven case: In that case, the detection is simply not sensitive to the other vibrational direction and the problem is purely one-dimensional, with no difference between the thermal and the e-beam noise being spectrally possible. Instead, one observes that even for small tilts of the measurement directions relatively to the eigenaxis of vibration, the composite signal becomes immediately and strongly sensitive to the aforementioned correlations, which materialize through spectral holes

being formed around frequencies that are determined by the combined mechanical and detection phases [10]: These strong spectral distortions are the signature of the presence of electron beam driving, and vice-versa. Overall, the absence of such distortions in the measured spectra indicates that the force noise induced by the electron beam is likely weaker than the thermal force noise of the nanotube.

8 Thermal versus driven response

In this section, we compare the piezo-driven response to the electromechanical spectrum obtained with device D4. The results are shown on Fig. S4. Fig. S4(a) shows the spectrum the electromechanical signal obtained as the fast Fourier Transform of the SEs current demodulated around 220 kHz. Two peaks are observed, with comparable heights and quality factors $Q_1 = 145$ and $Q_2 = 86$, respectively. These resonant peaks are in good agreement with those found from the piezo-driven response (Fig. S4(b)) which yields to two peaks as well, with quality factors $Q_1 = 205$ and $Q_2 = 70$. We attribute the slight unbalance of the two peaks to the orientation of the piezo-induced inertial force, which is rather aligned in the direction of the second vibrational mode. Note the presence of an anti-resonance at intermediate frequencies, resulting from a negative interference between the two mode. This is perfectly captured by the theoretical adjustment, which corresponds to the coherent sum of two resonant Lorentzian curves.

9 Amorphous carbon deposition in limited vacuum conditions

In presence of residual gas atmosphere, electron beam exposure is known to catalyze matter deposition [11]. To quantitatively determine the impact of a prolonged e-beam exposure on the mechanical properties of the carbon nanotube resonator, we proceed as follows. We set the SEM in spot mode and expose the sample for a given time. We subsequently determine both motion variance and mechanical resonance frequency using the calibration procedure described above. The results are shown on Fig. S5 and have been obtained with device D5 ($k = 3.7 \times 10^{-6} \text{ Nm}^{-1}$, $m_{\text{eff}} \simeq 52 \text{ ag}$). Figure S5(a) shows the scanning SEs images obtained at the beginning (left, $t = 0 \text{ s}$) and at the end (right, $t = 200 \text{ s}$) of the exposure. A clear deposition can be observed at the upper end of the carbon nanotube, where the electron beam spot has been set during exposure. Figures S5(b) and S5(c) show the evolution of the thermal variance and mechanical resonance frequency as functions of the exposure time. The thermal variance is found to be essentially invariant in time, suggesting no change in the restoring properties of the carbon nanotube resonator. In contrast, the mechanical resonance frequency decreases as a function of exposure duration, consistent with the increase of the effective mass. Figures S5(d) and S5(e) show the same results as S5(b) and S5(c) expressed in terms of the lateral spring constant and effective mass. In particular, Fig. S5(e) enables to determine a (linear) deposition rate of 0.8 ag s^{-1} . We have verified that this deposition rate can be decreased to much lower values at lower pressure and by carefully eliminating hydrocarbon molecules from the vacuum chamber.

References

- [1] Treacy, M. J., Ebbesen, T. & Gibson, J. Exceptionally high young's modulus observed for individual carbon nanotubes (1996).
- [2] Babic, B., Furer, J., Sahoo, S., Farhangfar, S. & Schönenberger, C. Intrinsic thermal vibrations of suspended doubly clamped single-wall carbon nanotubes. *Nano Letters* **3**, 1577–1580 (2003).
- [3] Krishnan, A., Dujardin, E., Ebbesen, T., Yianilos, P. & Treacy, M. Young's modulus of single-walled nanotubes. *Physical Review B* **58**, 14013–14019 (1998). URL <http://link.aps.org/doi/10.1103/PhysRevB.58.14013>.
- [4] Stipe, B. C., Mamin, H. J., Stowe, T. D., Kenny, T. W. & Rugar, D. Noncontact friction and force fluctuations between closely spaced bodies. *Phys. Rev. Lett.* **87**, 096801 (2001).
- [5] Gavartin, E., Verlot, P. & Kippenberg, T. J. Stabilization of a linear nanomechanical oscillator to its thermodynamic limit. *Nature communications* **4** (2013).
- [6] Moser, J., Eichler, A., Güttinger, J., Dykman, M. & Bachtold, A. Nanotube mechanical resonators with quality factors of up to 5 million. *Nature nanotechnology* (2014).

- [7] Gloppe, A. *et al.* Bidimensional nano-optomechanics and topological backaction in a non-conservative radiation force field. *Nature nanotechnology* **9**, 920–926 (2014).
- [8] Gil-Santos, E. *et al.* Nanomechanical mass sensing and stiffness spectrometry based on two-dimensional vibrations of resonant nanowires. *Nature nanotechnology* **5**, 641–645 (2010).
- [9] Niguès, A., Siria, A. & Verlot, P. Dynamical backaction cooling with free electrons. *Nature communications* **6** (2015).
- [10] Caniard, T., Verlot, P., Briant, T., Cohadon, P.-F. & Heidmann, A. Observation of back-action noise cancellation in interferometric and weak force measurements. *Physical review letters* **99**, 110801 (2007).
- [11] Ding, W. *et al.* Mechanics of hydrogenated amorphous carbon deposits from electron-beam-induced deposition of a paraffin precursor. *Journal of Applied Physics* **98**, 014905 (2005).

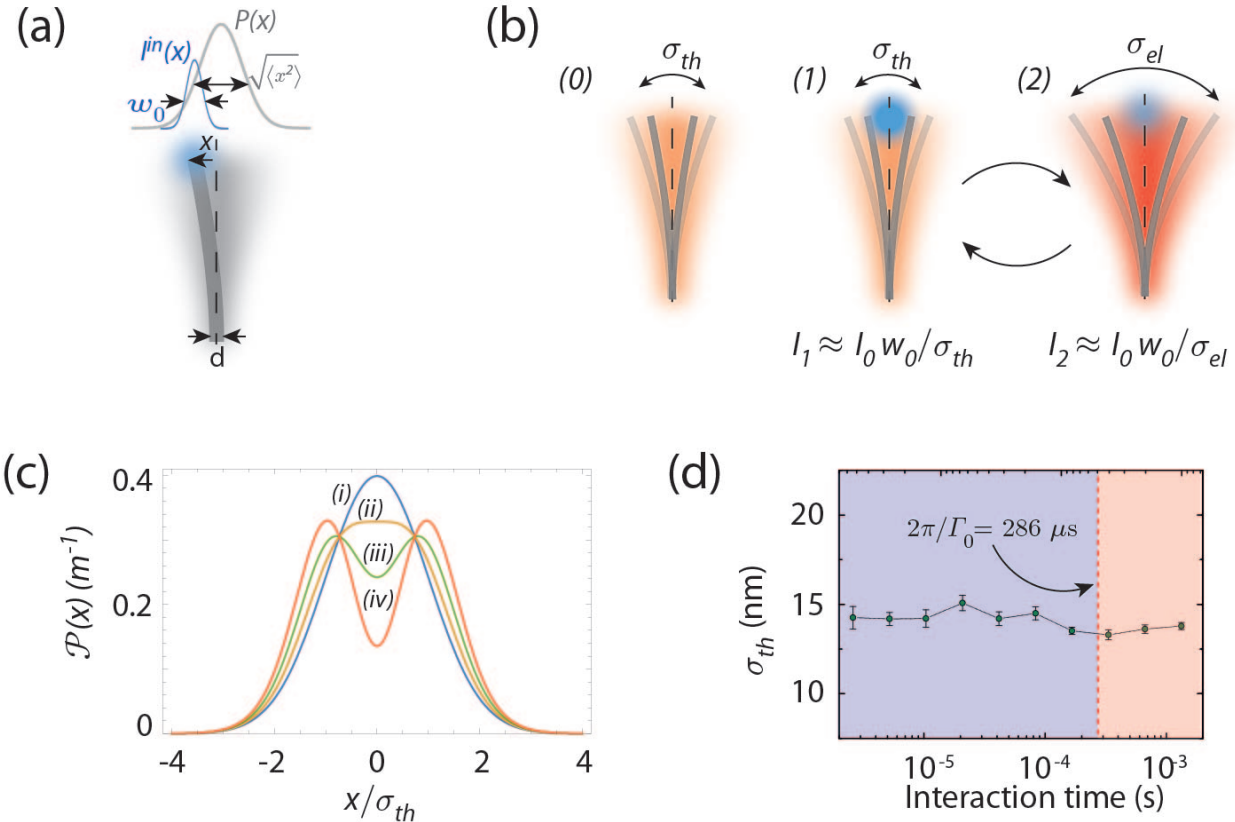


Figure S1: Effect of the e-beam on the motion PDF in scanning mode

(a) Schematic representing the geometric quantities of interest. (b) Schematic illustrating the expected multistable behaviour of the nanotube resonator under e-beam excitation. Initially resting at thermal equilibrium (0), the nanotube resonator is exposed to the electron beam at the centre of its Gaussian thermal trajectory, where its presence probability is maximum (1). This exposure yields to a strong mechanical excitation, resulting in a large increase of the motion variance (2). As a consequence, the presence probability is strongly reduced in the central region, resulting in a strongly reduced e-beam exposure. The nanotube resonator therefore returns to its thermal equilibrium, where it becomes again sensitive to e-beam excitation. (c) Calculated motion PDF of an e-beam driven nanotube resonator. The e-beam strength is defined relative to the thermal noise by the parameter ξ_e (see main text), with $\xi_e = 0$ (i), $\xi_e = 0.5$ (ii), $\xi_e = 1$ (iii), $\xi_e = 1.5$ (iv). (d) Motion variance as a function of the e-beam interaction time, defined as the time required for scanning a distance equivalent to the thermal standard deviation σ_{th} . Each point is obtained by fitting the corresponding second electron image using a Gaussian distribution. Dashed line separates the interaction time smaller and greater than the mechanical decay time $2\pi/\Gamma_0 = 286 \mu s$ (left and right, respectively.)

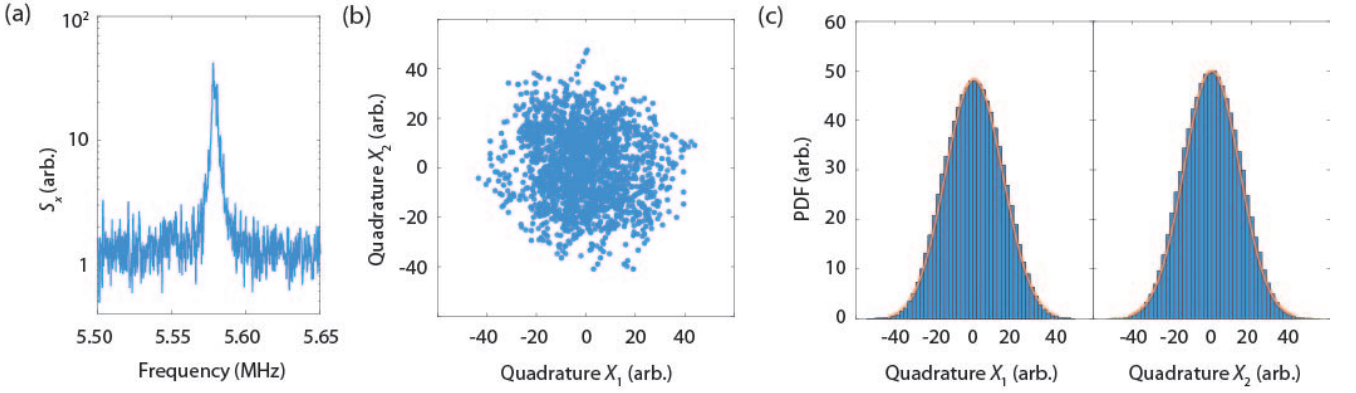


Figure S2: **One dimensional Brownian motion of a carbon nanotube resonator (device D1).** (a) Displacement power spectrum of the in-plane fundamental mode. (b) Corresponding motion quadratures represented in the phase-space. (c) Quadrature histograms, showing Gaussian distributions.

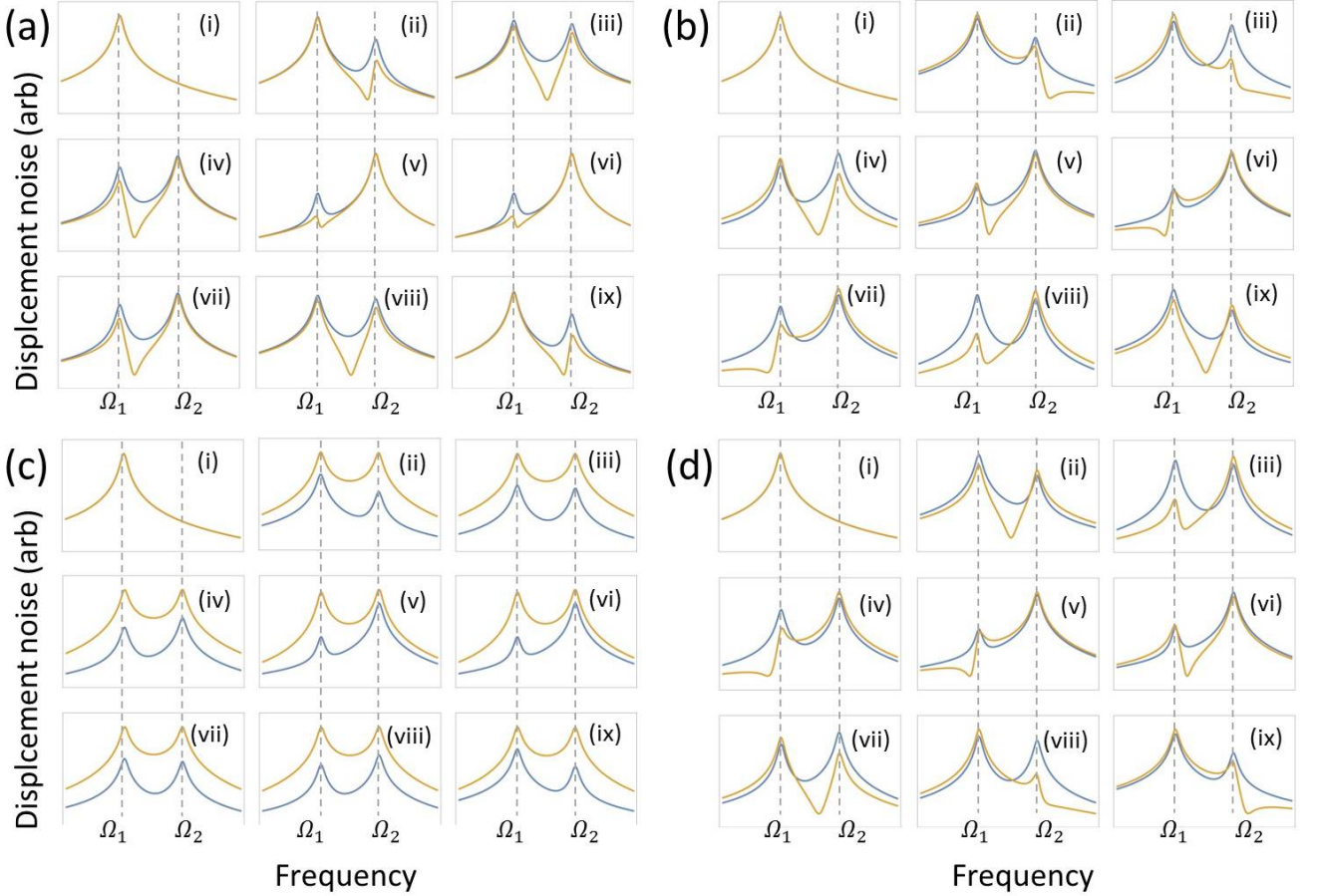


Figure S3: **Composite detection spectrum in presence of electron beam induced driving.** The composite spectrum $S_\theta[\Omega]$ (Eq. 29) is computed for 4 different force backaction orientations, $\beta = 0^\circ, 45^\circ, 90^\circ$, and 135° from (a) to (d). For each subset, both the thermal spectrum ($S_F^{\text{el}} = 0$, in blue) and the full composite spectrum (yellow) are plotted for various values of the angle θ , from $\theta = 0^\circ$ to $\theta = 160^\circ$ from (i) to (ix). The parameters used for evaluating Eq. 29 are $S_F^{\text{el}} = 100S_F^{\text{th}}$, $\Gamma_1 = \Gamma_2$, and $\Omega_2 - \Omega_1 = 10\Gamma_1$

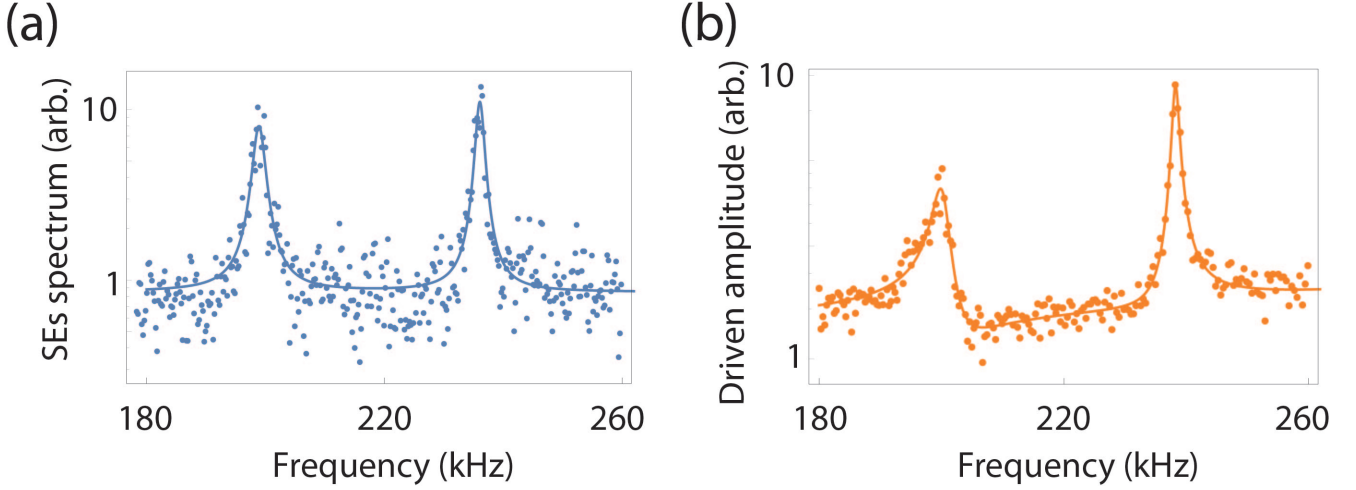


Figure S4: **2-dimensional incoherent and coherent response of a carbon nanotube resonator (device D4).** (a) Thermal spectrum obtained as the fast Fourier transform of the electromechanical signal. (b) Piezo-driven response acquired using the ultra-fast lock-in amplifier.

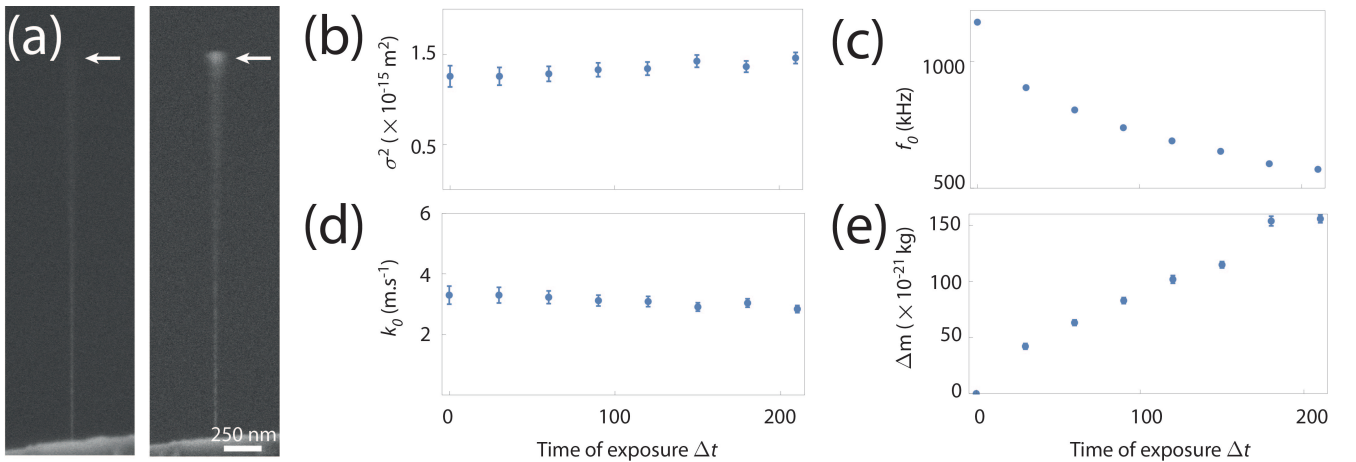


Figure S5: **Amorphous Carbon Deposition in Limited Vacuum Conditions (device D5).** (a) SEs images showing the nanotube resonator at the beginning (left) and at the end (right) of the prolonged exposure sequence. (b) Evolution of the motion variance (as measured in scanning mode) as a function of exposure time. (c) Evolution of the mechanical resonance frequency (as measured in spot mode through the thermal response) as a function of exposure time. (d) Evolution of the lateral spring constant as deduced from (b), through the expression $k = k_B T / \sigma_{\text{th}}^2$. (e) Evolution of the effective mass as deduced from $m_{\text{eff}} = k_B T / \sigma_{\text{th}}^2 \Omega_0^2$.